

Northumbria Research Link

Citation: Mathew, Derick, Chinnappa Naidu, Rani, Wang, Yue and Busawon, Krishna (2021) Single-stage microinverter with current sensorless control for BIPV system. IET Renewable Power Generation, 15 (11). pp. 2468-2479. ISSN 1752-1416

Published by: Institution of Engineering and Technology

URL: <https://doi.org/10.1049/rpg2.12177> <<https://doi.org/10.1049/rpg2.12177>>

This version was downloaded from Northumbria Research Link:
<http://nrl.northumbria.ac.uk/id/eprint/45972/>

Northumbria University has developed Northumbria Research Link (NRL) to enable users to access the University's research output. Copyright © and moral rights for items on NRL are retained by the individual author(s) and/or other copyright owners. Single copies of full items can be reproduced, displayed or performed, and given to third parties in any format or medium for personal research or study, educational, or not-for-profit purposes without prior permission or charge, provided the authors, title and full bibliographic details are given, as well as a hyperlink and/or URL to the original metadata page. The content must not be changed in any way. Full items must not be sold commercially in any format or medium without formal permission of the copyright holder. The full policy is available online: <http://nrl.northumbria.ac.uk/policies.html>

This document may differ from the final, published version of the research and has been made available online in accordance with publisher policies. To read and/or cite from the published version of the research, please visit the publisher's website (a subscription may be required.)



**Northumbria
University**
NEWCASTLE



UniversityLibrary

Single-stage microinverter with current sensorless control for BIPV system

Derick Mathew¹  | Rani Chinnappa Naidu¹ | Yue Wang² | Krishna Busawon³

¹ Electrical Engineering, VIT University, Vellore, Tamil Nadu, India

² Department of Engineering, University of Chichester, West Sussex, UK

³ Mechanical and Construction Engineering, Northumbria University, Newcastle upon Tyne NE1 8ST, UK

Correspondence

Rani Chinnappa Naidu, Electrical Engineering, VIT University, Vellore, Tamil Nadu, India.
Email: cran@vit.ac.in

Abstract

Building Integrated Photovoltaic (BIPV) microinverter system needs lower component counts and high efficiency at low power levels. In this context, this paper proposes a single-phase Transformerless Single-stage Buck-Boost Microinverter with sensorless control for the Grid-integrated BIPV system. The current estimation strategy is used to control the PV system, which reduces the costs and volume of the system. The leakage current of the system is reduced within the limits. It operates at a high level of efficiency, using an optimized number of active and passive components. In the absence of shoot-through problems, reliability is high for the proposed topology. MATLAB/Simulink simulation with a laboratory experimental setup for the proposed inverter for the First Solar BIPV module is designed to validate the results. Finally, the proposed inverter was compared to different Buck-Boost inverters at a power level of 70 W.

1 | INTRODUCTION

The prime motivation of the Building Integrated Photovoltaic (BIPV) system is the net-zero energy building and the reduction of CO₂ emissions by the construction industry. Recent market studies on BIPV system estimated an annual global compound growth rate of around 40% from 2009 to 2020 [1], [2]. The development of low-cost production methods for thin-film PV modules will further accelerate this growth. BIPV systems thus become architectural elements requiring features such as smaller size, ease of coupling to the grid system and the ability to capture maximum energy in all the environmental conditions. High efficiency and miniaturized inverters are required to meet these needs. Microinverter based approach is an optimal technique for BIPV applications [3], [4].

There are ample number of microinverters for PV modules available in the market [5]. However, it can be observed that isolated systems which are usually used increases size, weight and cost of the system. Another common configuration is multiple stage inverters, which reduces efficiency and lifetime [6]. The maximum efficiency of commercially available microinverters ranges from 85% to 95% at its maximum power [7]. Alternative technique is single-stage transformerless microinverters, which are designed with high efficiency [8].

Various single-stage topologies have been reviewed in [9]. In this area of research, there are different divisions based on the boost derived and the buck-boost derived topologies. In [10], differential boost inverter is presented, in which two boost converters produces a sinusoidal waveform shifted by 180°. The main drawback of this topology is high-frequency switches are hard switched, causing electromagnetic interference problems and high switching losses. Boost microinverter described in [11] is specifically designed as a microinverter for rooftop solar PV system; however, owing to the use of bulky inductors, the topology was not suitable for the BIPV applications. The inverter presented in [12] uses the idea of a charge-pump model based on capacitor circuit to boost the voltage. It is double grounded to eliminate the leakage current. However, its Maximum Power Point Tracking (MPPT) control is difficult due to non-symmetric input current. Based on the doubly grounded principle, the half bridge buck-boost inverter was presented in [13]. Two PV modules are connected to two converters that are connected in parallel. Although it has low losses, there are few drawbacks mainly due to the injection of asymmetric current into the grid, which shows a high THD and a high voltage ripple across the DC link capacitors, which reduces the accuracy of the MPPT. In [14], an inverter with four bi-directional switches was introduced. Control of this inverter is highly complex because

This is an open access article under the terms of the [Creative Commons Attribution](https://creativecommons.org/licenses/by/4.0/) License, which permits use, distribution and reproduction in any medium, provided the original work is properly cited.

© 2021 The Authors. *IET Renewable Power Generation* published by John Wiley & Sons Ltd on behalf of The Institution of Engineering and Technology

the modes of operation of the inverter are different for duty ratio less than and greater than 0.5; the static gain characteristic of the inverter is non-linear as a result of which the output voltage is distorted. The active buck-boost inverter topology with a reduced number of passive components is presented in [15]. Topology can be divided into DC-AC inverter and AC-AC module, where the former performs buck operation and the latter performs boost operation. Interleaved flyback topology has been used in [16]. One of the main highlight of this topology is the use of Discontinuous Conduction Mode (DCM) operation of inductor. The benefits of DCM are listed as follows: dynamic response is fast, stability is assured, reverse recovery can be neglected, no power loss during turning ON and easy to control. High gain single-stage inverter topology based on coupled inductor is presented in [17]; the main advantage of this configuration is that the component count is lower, and high voltage gain and additional capacitors are not required to capture leakage energy. A quasi single-stage buck-boost inverter is developed in [18]. The significance of this topology is as follows: current shoot through is eliminated, DC link capacitor is removed and resistant to current flow through body diodes of MOSFETS, but the cost and volume of the topology is high as it uses the series of diodes with all MOSFET. Additionally, inductor counts in this scheme are more compared to other topologies. A CUK-derived inverter topology is given in [19]. It presents a configuration with negative terminal of PV module and grid neutral are always connected together. This precludes ground leakage current effectively. The configuration includes additional capacitor and inductor which increases the order of the system, as well as control complexity. The same principle of grounding is used in [20]. It is a DCM-operated inverter (DCMI), with a flying inductor to buck-boost the voltage. In [21], similar technique is utilized to prevent common mode voltage. It uses two circuits, that work together to synthesis two halves of output voltage. These bimodal operations of the inverter can result in distortion in output voltage. Control complexity will be high to restrict the harmful effects of bimodal action.

With the comprehensive literature study carried out so far, the design of a single-stage microinverter with the following features together draws attention:

1. Buck-Boost inverters with a lower number of conduction devices to reduce losses, size and heat dissipation.
2. Use of optimized number of sensor reduces cost, volume of the system.
3. Leakage current within the normal limit decreases the impact of EMI and harmonic distortion.
4. Higher efficiency in lower power ranges.
5. Protection from shoot-through problems.

In this context, this paper proposes a Transformerless Single-Stage Buck-Boost Microinverter (TSBBM) topology. It uses a sensorless control for Pulse Width Modulation (PWM) by current estimation, eliminating two expensive current sensors. Overall, the total system incorporates all of the above mentioned vital requirements. Various new and

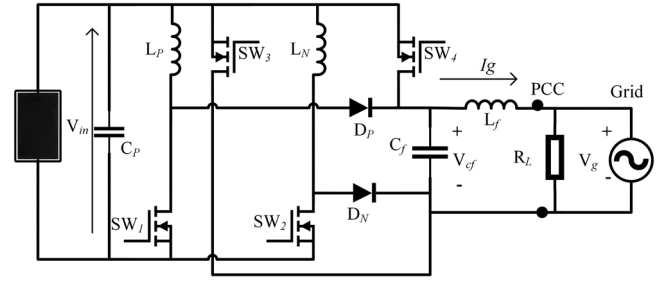


FIGURE 1 Schematic diagram of the TSBBM

scientific contributions to the BIPV system have been described for the first time in this research:

1. TSBBM topology with less number of active and passive components in conduction path.
2. Sensorless control technique using the current estimation technique.
3. Attained higher efficiency in lower power range with less number of active switches. formerless
4. Limited the leakage current with in the limit.

2 | CIRCUIT DESCRIPTION AND OPERATING PRINCIPLE

Figure 1 demonstrates the proposed TSBBM topology, with four semiconductor switches, two diodes and a filter capacitor. The L_p and L_N inductors have been used for buck-boost operation. In addition, they prevent shoot-through issues in the inverter. This increases the system reliability and reduces switching operation complexity. Switches SW_1 and SW_2 are switched on to charge L_p and L_N inductors during positive and negative half cycles of the reference signal respectively. The switches SW_3 and SW_4 plays a significant part in the discharge of inductors energy into the grid. The switches SW_1 and SW_2 operates at high frequency while the switches SW_3 and SW_4 operates at low frequency. There are six modes of operation for the inverter, three of which occur continuously in the positive half of the reference cycle, and the other three in the negative half of the reference cycle. In general, the inverter is identical to the conventional buck-boost converter in both half of the reference cycles, where the difference is that the proposed inverter modulates on a quasi-sinusoidal duty cycle.

The three modes of operation in the positive half-cycle and negative half-cycle remains the same with the use of different switches. The equivalent circuits of three modes in the positive half-cycle of the reference cycle are shown in Figure 2. It is important to note that only one switch is used in the conduction path during each operation, even if another switch is on. This will potentially reduces the overall system power loss.

Mode P_1 : As illustrated in Figure 2(a), the P_1 operating mode is used for the current imposition of the L_p inductor, switch SW_1 is enabled for this purpose. The interruption of the leakage current path occurs, due to the high impedance offered. The

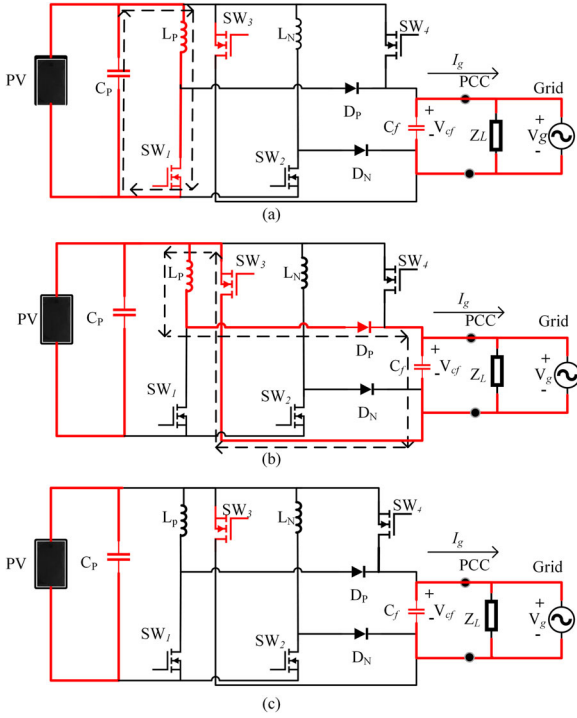


FIGURE 2 Equivalent circuits for (a) Mode P_1 , (b) Mode P_2 , (c) Mode P_3

following differential equations are derived from the Figure 2(a).

$$\frac{di_{L_p}(t)}{dt} = \frac{V_i}{L_p}, \quad (1)$$

$$\frac{dv_{C_f}(t)}{dt} = \frac{v_g(t)}{C_f R_L}. \quad (2)$$

Here, V_i and V_g are the input voltage and grid voltage, respectively; I_{L_p} and V_{C_f} are the current through inductor L_p and the voltage across capacitor C_f , respectively; and R_L is the load resistance.

Mode $P_2:P_2$ operating mode begins after storing the appropriate energy in inductor L_p to achieve the necessary voltage gain. In this mode, the energy stored is discharged to the filter capacitor and load. SW_1 is triggered off, mean while diode D_p becomes forward-biased and forms a conduction path through SW_3 and inductor L_p . Following differential equations are derived from Figure 2(b).

$$\frac{di_{L_p}(t)}{dt} = \frac{v_{C_f}(t)}{L_p}, \quad (3)$$

$$\frac{dv_{C_f}(t)}{dt} = \frac{i_{L_p}(t)}{C_f} - \frac{v_g(t)}{C_f R_L}. \quad (4)$$

Mode $P_3:P_3$ mode starts when all the energy in the inductor L_p is transferred to the capacitor C_f . In this mode, energy from the output filter capacitor is transferred to the load as shown in Figure 2(c).

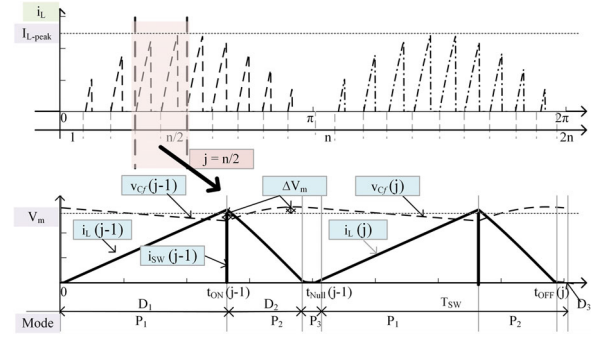


FIGURE 3 Inductor current and capacitor voltage for analysis during the peak switching interval

$$\frac{dv_{C_f}(t)}{dt} = -\frac{v_g(t)}{C_f R_L}. \quad (5)$$

The devices in the conduction path are highlighted in each mode and the direction of current flow is shown with the dashed lines in Figure 2.

3 | THEORETICAL ANALYSIS OF THE TOPOLOGY

The following assumptions are taken for the evaluation of the proposed topology:

1. The relationship between fundamental frequency F_g and switching frequency F_{SW} is $F_{SW} = 2n \times F_g \forall n \in \mathbb{N}$.
2. The characteristics of the semiconductor devices are ideal.
3. Grid voltage $v_g(t)$ is constant during each switching time period T_{SW} .
4. The forward resistance is zero and reverse resistance is infinite for MOSFETs and Diodes.
5. The value of the duty ratio is constant over a switching period T_{SW} .
6. Discontinuous Conduction Mode (DCM) operation is maintained throughout the operation of the inverter.

The discontinuous current I_{L_p} and I_{L_N} of inductors L_p and L_N are shown in Figure 3. Since both inductors operates in the same way during positive and negative cycles, they are commonly represented as L in the analysis section. From (1) and (3), the voltage gain is obtained as given in (6). Inductor current increases in P_1 mode, from Figure 3 inductor charging current I_L hits its peak value at the instant $t = t_{ON}(j)$ for j^{th} switching period. The peak value of the current I_{L-Peak} is specified in (7), it depends on the output power, because the amount of energy transmitted to the output is determined by the magnetizing current of the inductor. The energy stored in the inductor E_{in} can be expressed as (8).

$$V_g = V_i \frac{D_1}{D_2}, \quad (6)$$

$$i_{L_peak}(j) = \frac{V_i}{L} D_1(j) T_{SW}, \quad (7)$$

$$e_{in}(j) = \frac{1}{2} L i_{L_peak}(j)^2. \quad (8)$$

Here, D_1 and D_2 are the on time and off time duty ratio. The average inductor current I_{avg} over a switching period can be formulated as (9). It is evident from the expression (9) that the output current I_g can be specified as a sinusoidally varying I_{avg} . Thus, energy at the output side E_{out} is formulated as in (10). The charging duty ratio can be expressed as (11) by equating the expressions (8) and (10), here M is the inverter modulation index.

$$i_{avg}(j) = \frac{i_{L_peak}(j) D_2}{2} \Rightarrow \frac{V_i^2 D_1(j)^2 T_{SW}}{2 L I_g(t)}, \quad (9)$$

$$e_{out}(j) = i_{avg}(j) V_m \sin^2\left(\frac{\pi}{n} j\right) T_{SW}, \quad (10)$$

$$D_1(j) = \sqrt{\frac{2 L I_{avg} V_m}{V_i^2 T_{SW}}} \sin\left(\frac{\pi}{n} j\right) \Rightarrow M \sin\left(\frac{\pi}{n} j\right). \quad (11)$$

3.1 | Requirement for DCM operation

DCM operation occurs, if the DC component of I_L is smaller than the maximum ripple. Across the whole grid cycle, the proposed inverter topology works in DCM mode, if it supports DCM requirements for peak time duration ($j = n/2$). In order to determine the maximum modulation index M limit for maintaining DCM operation, the critical conduction mode condition for peak sampling duration ($j = n/2$) of the grid cycle is applied. With respect to these requirements, the maximum modulation index limit is determined as given in(12).

$$M_{max} = \frac{V_m}{V_i + V_m}. \quad (12)$$

Here, V_m is the peak output voltage.

3.2 | Design of energy storage elements

As the inverter operates in DCM, energy is transferred in a discrete form. Inductor L stores and transfers energy during each switching period T_{SW} from the PV module to the load. So, in order to filter this discrete form, the capacitor C_f is used in the topology. This means that the energy stored in the inductor is completely transferred to C_f . The maximum amount of energy is transferred from L to C_f during the peak period $j = n/2$. If P_{max} is the maximum input power, the inductor should have the capacity to handle $2P_{max}$. This condition ensures that the average power P_{max} is delivered to the grid during each grid

cycle so, (13) is formulated from (8). The inductor value can be determined using equation (14) by substituting (7) in (13). The design value of L is determined based on the maximum power level of PV module.

$$\frac{1}{2} L I_{L_peak}(n/2)^2 = 2 V_{gRMS} I_{gRMS} T_{SW}, \quad (13)$$

$$L = \frac{V_i^2 t_{ON}^2 (n/2)}{4 P_{max} T_{SW}} \Rightarrow L \leq \frac{V_i^2 M_{max}^2 T_{SW}}{4 P_{max}}. \quad (14)$$

The filter capacitor C_f is designed based on the changes in capacitor energy throughout $D_2 T_{SW}$, which can be expressed as (15) and thus the design value can be stated as (16).

$$2 P_{max} T_{SW} = \frac{C_f [(V_m + \Delta V_m)^2 - (V_m - \Delta V_m)^2]}{2}, \quad (15)$$

$$C_f = \frac{P_{max} T_{SW}}{V_m \Delta V_m}. \quad (16)$$

Here, ΔV_m is the ripple voltage.

3.3 | Design of DC-link capacitor (C_p)

In a single-phase grid-connected microinverter model, the double-line frequency issue is general, that is, the power generated from the PV panel must be at the maximum power point while the power required by the grid varies for time. It is necessary to place the decoupling capacitor in order to ensure power balancing. The injected power into the grid and input power is given in (17). So, the decoupling capacitor (C_p) design equation can be derived as (18).

$$P_{out} = 2 P_{max} \sin^2 \omega t, \quad (17)$$

$$C_p = \frac{P_{max}}{2\pi f_g V_i \Delta V_{PV}}, \quad (18)$$

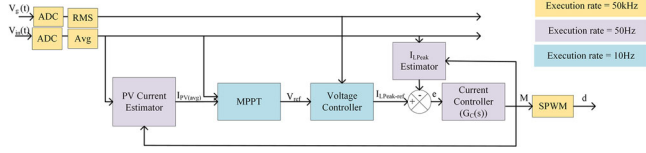
Here, ΔV_{PV} is the PV ripple voltage.

3.4 | Selection of power device

The rating of the power devices influences the overall cost and the performance of the system. This ensures that the voltage and current stress on power devices must be calculated. The maximum break down voltage rating of the MOSFET is greater than the maximum difference between the input voltage and output voltage. If the inverter comprises k number of switching devices, that the total active switch stress SS is defined based on RMS current I_{RMS_i} and V_{max} as given in (19). The expressions for I_{RMS_i} and V_{max} of all switches in the topology are listed in Table 1.

TABLE 1 RMS current and peak voltage expressions

	SW_1, SW_2	SW_3, SW_4	D_P, D_N
I_{RMS}	$\frac{V_i T_{SW}}{3L} \sqrt{\frac{M^3}{\pi}}$	$\frac{T_{SW}}{2L} \sqrt{\frac{V_i^2 M^3}{6V_m}}$	$\frac{T_{SW}}{2L} \sqrt{\frac{V_i^2 M^3}{6V_m}}$
V_{max}	$V_i + V_m$	V_m	V_m


FIGURE 4 Block diagram of the sensorless control technique

$$SS = \sum_{i=1}^k V_{max} I_{RMS_i}. \quad (19)$$

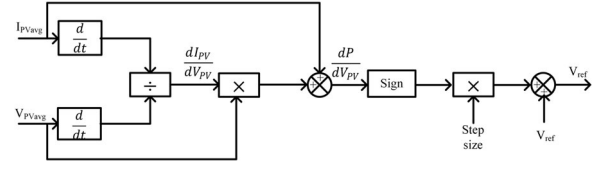
4 | SENSORLESS CONTROL TECHNIQUE

The sensorless control technique based on current estimation strategy consists of four modules, the PV current estimator, the peak average inductor current estimator, the voltage controller and the current controller. The detailed block diagram is presented in Figure 4.

4.1 | Sensorless MPPT

As the power, voltage and current of the PV modules shows non-linear characteristics, the maximum power of the PV module cannot be extracted by linear control techniques. Perturbation and observation (P&O) and Incremental Conductance (*InC*) methods are the most common non-linear MPPT control methods [22]. So, Perturbation and observation (*P&O*) MPPT technique is used in this project. In this method, the operating point is controlled by either increasing or decreasing the PV voltage to its Maximum Power Point (MPP). Generally, MPPT operation is done using current and voltage sensors, which increases the cost and the volume of the system. An alternative MPPT method without a current sensor, but estimating it using the relation between the input and output voltage is proposed in this work. From Figure 1, Equation (20) is formulated. From Figure 3, the average current through the switch I_{SW} can be written as (21). The average current through the coupling capacitor I_{C_p} is given in (22). The average PV current $I_{PV}(avg)$ can therefore be formulated as (23). Estimated $I_{PV}(avg)$ and sensed V_{PV} are used in *P&O* method for MPPT as shown in the Figure 5. After several iterative study optimized 10Hz MPPT frequency is used in the project.

$$I_{PV_{avg}} = I_{SW_{avg}} + I_{C_{p_{avg}}}, \quad (20)$$


FIGURE 5 Block diagram for Perturbation and observation (*P&O*) Algorithm

$$I_{SW_{avg}} = \frac{\sum_{j=1}^{2n} I_{L_{Peak_{max}}} M \sin^2\left(\frac{\pi}{n} j\right)}{2n}, \quad (21)$$

$$I_{C_{p_{avg}}} = F_g C_p \Delta V_{in}, \quad (22)$$

$$I_{PV_{avg}} = \frac{V_{in} M^2}{4L F_{SW}} + F_g C_p \Delta V_{in}, \quad (23)$$

$$\frac{dP}{dV_{in}} = I_{PV} + V_{in} \frac{dI_{PV}}{dV_{in}}. \quad (24)$$

4.2 | Voltage controller

The voltage controller determines the output peak current reference $I_{g_{Peak_{ref}}}$, depending on the power extracted from the PV module. In order to simplify, the input power P_{PV} is assumed to be equals to the output power P_g , by neglecting the losses, and (25) is formulated. Since the relationship between the grid injected current $I_{g_{Peak}}$ and the modulation index M depends on the inductor current $I_{L_{Peak}}$. It is therefore necessary to identify the peak inverter current reference $I_{L_{Peak_{ref}}}$. It is determined from the (9) at $j = n/2$ but the unknown variable D_2 need to be identified. From (11) D_1 at $n/2$ and I_{avg} as $\frac{V_m}{R_L}$ can be solve as given in the (26). So, by comparing (26) and (7), D_2 can be equated as in (27). While substituting (27) and (25) in (9), $I_{L_{Peak_{ref}}}$ is obtained as (28). Since R_L varies in practical case, so it is identified in terms of $\frac{P}{V_{RMS}^2}$.

$$I_{g_{Peak_{ref}}} = \frac{2I_{PV_{avg}} V_{ref}}{V_m}, \quad (25)$$

$$\frac{V_g}{V_{in}} = \frac{D_1}{\sqrt{\frac{2L}{R_L T_{SW}}}}, \quad (26)$$

$$D_2 = \sqrt{\frac{2L}{R_L T_{SW}}}, \quad (27)$$

$$I_{L_{Peak_{ref}}} = I_{g_{Peak_{ref}}} V_m \sqrt{\frac{T_{SW}}{V_{ref} I_{PV_{avg}} L}}. \quad (28)$$

4.3 | Current estimator and current controller

The current estimator and controller use the inductor energy conservation principle. From (7), the peak inductor current is

TABLE 2 State variable expressions of the topology at different mode

	Mode P_1 (D_1)	Mode P_2 (D_2)	Mode P_3 (D_3)
V_L	V_i	V_{C_f}	0
I_{C_f}	$-\frac{V_{C_f}}{R_L}$	$I_L - \frac{V_{C_f}}{R_L}$	$-\frac{V_{C_f}}{R_L}$

estimated. For current controller, inductor current I_L and capacitor voltage V_{C_f} are considered as state variables. The state variable expressions during different operating modes are shown in Table 2. Addition of perturbation signal to the steady-state values of the duty cycle and state variables are presented in (29).

$$\begin{aligned} i_L &= I_L + \tilde{i}_L, v_{C_f} = V_{C_f} + v_{C_f}^{\tilde{}} \\ D_1 &= D_{10} + \tilde{d}_1, D_2 = D_{20} + \tilde{d}_2 \end{aligned} \quad (29)$$

Here, I_L , V_{C_f} , D_{10} , D_{20} are the steady state values and \tilde{i}_L , $v_{C_f}^{\tilde{}}$, \tilde{d}_1 , \tilde{d}_2 are the perturbation signals. The input voltage perturbation is ignored since the objective is to acquire control D to I_L transfer function. Small signal model of the inverter is represented in matrix form in (30). The system transfer function $G_i(s)$ is given in (31).

$$\frac{d}{dt} \begin{bmatrix} \tilde{i}_L \\ v_{C_f}^{\tilde{}} \end{bmatrix} = \begin{bmatrix} 0 & \frac{D_{20}}{L} \\ \frac{D_{20}}{C_f} & -\frac{1}{R_L C_f} \end{bmatrix} \begin{bmatrix} \tilde{i}_L \\ v_{C_f}^{\tilde{}} \end{bmatrix} + \begin{bmatrix} \frac{2V_i}{V_{C_f}} \\ \frac{I_L V_i}{V_{C_f}} \end{bmatrix} \tilde{d}, \quad (30)$$

$$G_i(s) = \frac{i_L^{\tilde{}}(s)}{d^{\tilde{}}(s)} = \frac{73s + 8.98 \times 10^5}{s^2 + 1.2 \times 10^4 s + 9.22 \times 10^6}. \quad (31)$$

The main objective of the current controller is to track the current reference precisely, to minimize a steady-state error. A Proportional and Integral controller (PI) is implemented to mitigate the steady-state error. The transfer function of the PI controller $G_c(s)$ is given in (33). The K_p and K_i are obtained as 652 and 20000, respectively, by using MATLAB PID tuner tool. The sensitive function S_i with respect to each parameter of the proposed inverter is defined as the change in inductor peak current ($I_{L_{peak}}$) at a fixed duty D_1 with respect to different parameters x_j . Inductor peak current depends on input voltage (V_i) and inductor (L). The sensitivity is calculated, at $D_1 = 0.67$ with system parameters, sensitivity with respect to V_i is 0.08 on the other hand it is highly sensitive to the variations in the inductance.

$$S_i = \frac{\partial I_{L_{peak}}}{\partial x_j}, \quad (32)$$

$$G_c(s) = K_p + \frac{K_i}{s}. \quad (33)$$

5 | LOSS ANALYSIS

The power-loss analysis of the TSBBM inverter is discussed in this section.

5.1 | Core loss

Core loss is caused within a material by the changing magnetic flux field. The core loss density (P_L) is a function of half the flux swing (ΔB) and the switching frequency (f_{SW}) as given in (34). Core loss charts can be approximated to identify constants such as a, b, and c.

$$P_L = a \frac{\Delta B^b}{2} f_{SW}^c \quad (34)$$

Here, flux swing ΔB is given in (35).

$$\Delta B = \frac{N \Delta I_{L_{avg}} \mu_0}{l_g}, \quad (35)$$

$$\Delta I_{L_{avg}} = \frac{I_{L_{peak}} \sum_{k=1}^n \sin\left(\frac{\pi k}{n}\right)}{n}. \quad (36)$$

Here, N is the number of turns, ΔI_L is the ripple current in the inductor and l_g is the air gap in the magnetic core. μ_0 is the permeability of the air gap which is $4\pi \times 10^{-7}$. So, the core loss is given in (37).

$$P_{core} = P_L l_e A_e, \quad (37)$$

Here, l_e is mean path length of the magnetic core and A_e is the cross sectional area.

5.2 | Conduction loss

The conduction loss is the sum of inductor conduction loss and power device conduction loss.

5.2.1 | Inductor conduction loss

Inductor conduction loss P_{cond_L} is based on the $I_{L_{avg}}$ and the series resistance of the inductor R_L as given in the (38).

$$P_{cond_L} = I_{L_{avg}}^2 R_L. \quad (38)$$

5.2.2 | Conduction loss of switching devices

In TSBBM, SW_3 and SW_4 operates in symmetrical manner in positive and negative half cycle so both of them is having same conduction losses, which is determined as given in (39).

$$P_{cond_{SW_{3,4}}} = I_{RMS_{SW_{3,4}}}^2 R_{ds}. \quad (39)$$

Similarly conduction loss through the switches SW_1 and SW_2 are given in the (41).

TABLE 3 Parameters for power loss calculation

Number of turns N	74
Permeability of air gap μ_o	$4\pi \times 10^{-7}$
Air gap in the magnetic core l_g	2 mm
Mean path length of magnetic core l_e	171.1 mm
Cross sectional area A_e	49 mm^2
Inductor resistance R_L	$6.75 \text{ m}\Omega$
ON state resistance of MOSFET R_{ds}	0.43Ω
ON state resistance of Diode R_{ak}	0.03Ω
Fixed voltage drop V_{FV}	1.5 V
Falling time t_f	4.5 ns
Turn OFF energy loss E_{OFF}	0.015 mW

$$P_{cond,SW_{1,2}} = I_{RMS,SW_{1,2}}^2 R_{ds}. \quad (40)$$

Here, expression for $I_{RMS,SW_{3,4}}$ and $I_{RMS,SW_{1,2}}$ are given in the Table 1.

A diode's conductive loss is calculated based on the power loss associated with the fixed voltage drop (V_{FV}) and resistive (R_{ak}) voltage, and is measured as (42).

$$P_{cond,D_{PN}} = I_{RMS,D_{PN}}^2 R_{ak} + I_{RMS,D_{PN}} V_{FV}. \quad (41)$$

Here, $I_{RMS,D_{PN}}$ is given in Table 1, R_{ak} and V_{FV} are determined from the datasheet of the diode.

5.3 | Switching loss

Since SW_3 and SW_4 are operating at low switching frequency, the switching loss of those switches is negligibly small. Similarly since, the inverter operate in DCM the switching loss of diode due to reverse recovery is zero. In switches SW_1 and SW_2 turn on losses is zero due to the DCM operation. So total switching losses of the inverter is given in (42).

$$P_{SW_{1,2}} = \frac{\langle V_{sw} \rangle_T \langle I_{sw} \rangle_T}{2} f_{sw} t_f + E_{OFF} f_{sw}. \quad (42)$$

Here, t_f is the fall time, E_{OFF} is the Turn OFF energy loss of the switch available in the datasheet. The losses of the inverter is calculated based on the parameters tabulated in the Table 3. In Table 4, the power loss of the TSBBM inverter operating in CCM and DCM shows that the topology efficiency is higher when operating in DCM. Based on the analytical calculation, the efficiency of the proposed topology is calculated to be 93.7 %. Comparing the TSBBM inverter with recently developed topologies, as shown in Figure 6, shows that the proposed topology is more efficient compared to most other topologies [23].

TABLE 4 Power loss of TSBBM inverter while operating in DCM and CCM operation

Losses	CCM	DCM
SW Conduction losses (W)	1.24	2.44
SW Switching losses (W)	1.5	5.18×10^{-3}
D Conduction losses (W)	0.93	0.72
Inductor core loss (W)	4.09	0.89
Inductor copper loss (W)	0.03	0.52

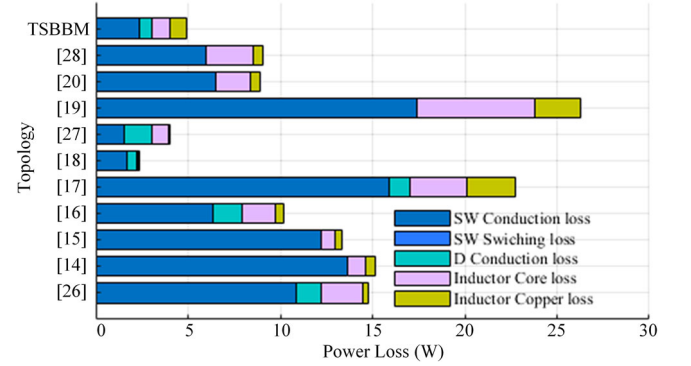


FIGURE 6 Comparison of loss breakdown of different microinverters

6 | DESIGN VALIDATION

6.1 | Simulation results

To verify the feasibility of the above theoretical analysis, the inverter is simulated in the MATLAB/Simulink software using the ratings and component values as shown in the Table 5. The First Solar FS 270 thin film PV module is used as a source, which is modelled using the methodologies presented in [24] and [25]. The inverter test control circuit is designed based on the block diagram shown in Figure 4.

TABLE 5 Values of the components used for modelling, simulation and experimental setup

Input parameters	$V = 73 \text{ V}, I = 0.96 \text{ A}$
Output parameters	$P_{max} = 70 \text{ W}, V_{RMS} = 110 \text{ V}$ $I_{RMS} = 0.63 \text{ A}, R_L = 172.8 \Omega$
Switching devices	$F_g = 50 \text{ Hz}$
	$F_{SW} = 50 \text{ kHz}$
	$0.314 \leq D \leq 0.669$
	MOSFET - FQP10N20C Diode - FEP30JP-4 Gate driver - TLP350
Inductor (L_p, L_N)	$160 \mu\text{H}, I_{L_{rak}} = 6.2 \text{ A}, R_{dc} = 14 \text{ m}\Omega$
Capacitor	$C_f = 0.47 \mu\text{F}, MPX2 250V_{AC},$ $C_p = 220 \mu\text{F}$

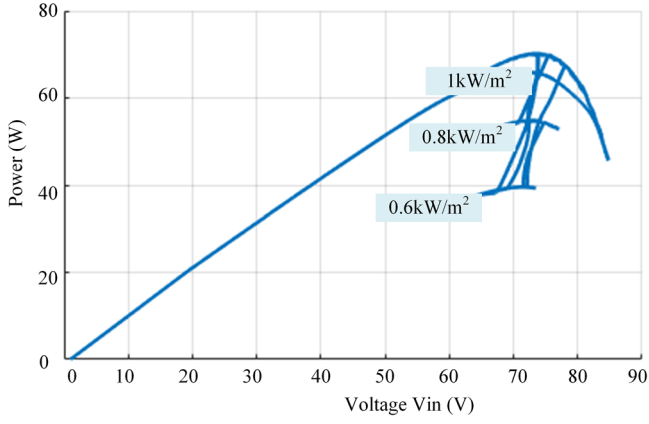


FIGURE 7 Input power versus voltage ($P - V$) curve

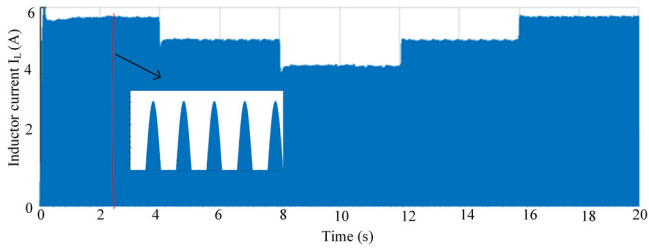


FIGURE 8 Variation of i_L during irradiance change

In the input, a step change in the level of irradiation was applied to analyze the reference tracking technique of the sensorless control of the proposed inverter. Figure 7 shows the MPPT operation while changing irradiation level from 0.8 kW/m^2 to 1 kW/m^2 at 1.25 s. It clearly indicates that the inverter operates at MPP field. Additionally, as the irradiation increases, the current derived from PV increases as shown in Figure 8. The effect of V_i with irradiation change is shown in Figure 9. As the irradiation level increases the current injected into the grid also increases as shown in Figure 10. Figure 11 exhibits shifts in output power during irradiation changes.

The resonant circuit is formed in a transformerless inverter as shown in Figure 12. The resonant circuit includes parasitic capacitance of PV (C_{PV}) and filter inductor (L_f). Here, X and Y are the terminals of the inverter which is connected to single phase grid through L_f . The inverter can therefore be

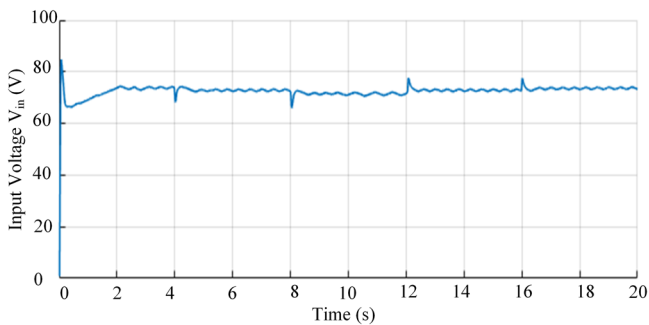


FIGURE 9 Variation in the input voltage V_i during irradiance change

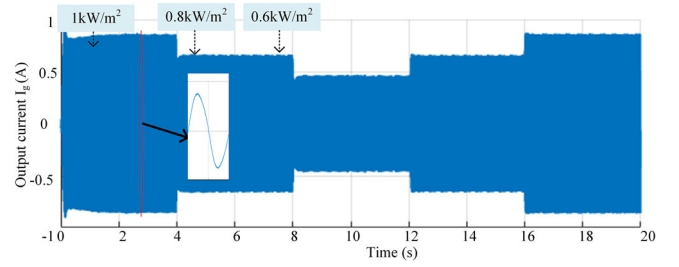


FIGURE 10 Change in the output current I_g during irradiance change

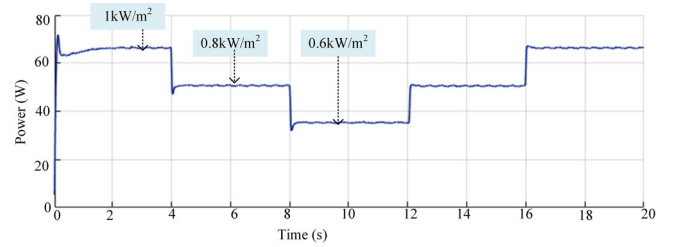


FIGURE 11 Variation in the active power (P) during irradiance change

standardized into an equivalent circuit consisting of V_{XN} and V_{YN} as shown in Figure 12. So, leakage current is a function of V_{XN} and V_{YN} . The Common Mode Voltage can be defined as (43) [26]. In the case of a V_{CM} difference, the leakage current flows through the parasitic capacitance and to the grid. In the proposed topology, V_{XN} and V_{YN} are low-frequency components as shown in Figure 13. The voltage difference between the ground of the BIPV module and that of the grid is low frequency so, that the equivalent impedance of the

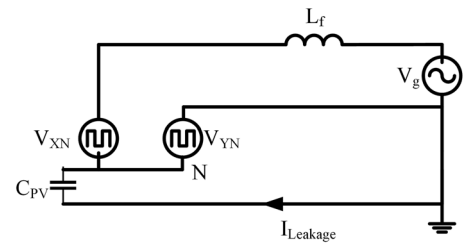


FIGURE 12 Equivalent circuit for TSBBM for showing leakage current path

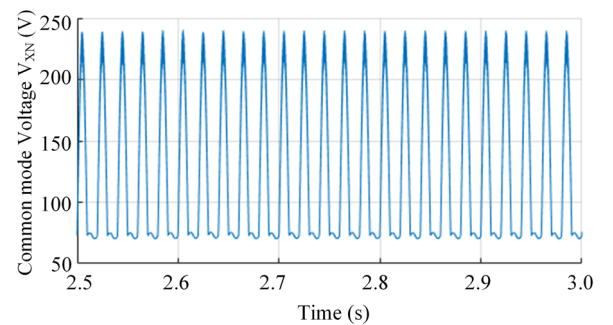


FIGURE 13 Common mode voltage Voltage V_{XN}

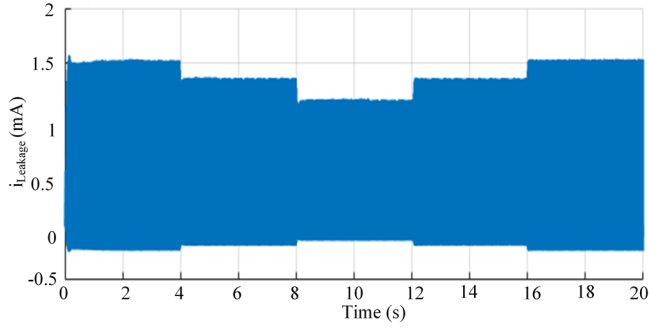


FIGURE 14 Variation of leakage current $i_{Leakage}$ during irradiance change

parasitic capacitance is high. This high impedance limits the flow of leakage current $I_{Leakage}$, as shown in the Figure 14. Here parasitic capacitance of $70nF$ was used in the simulation to check the leakage current flow for the proposed inverter [27]. As German standards DIN VDE 0126-1-1, inverter must be disconnected from the grid if the RMS value of leakage current $i_{Leakage}$ reaches $30 mA$. Figure 14 indicates that leakage current of the proposed inverter is negligibly small.

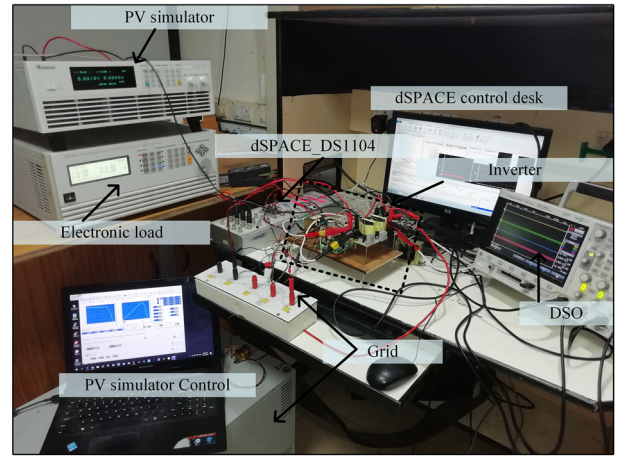
$$V_{CM} = \frac{V_{XN} + V_{YN}}{2}. \quad (43)$$

6.2 | Experimental results

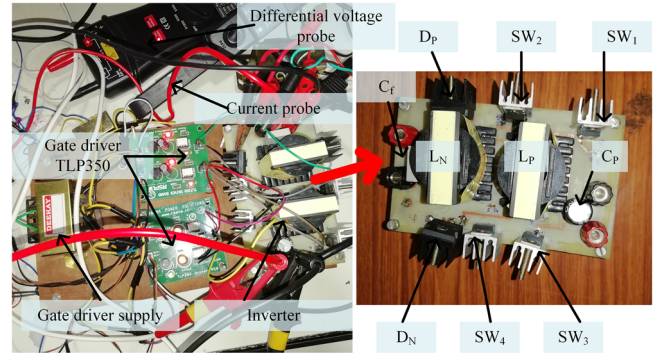
An experimental model of 70 W, 110 V, 50 Hz inverter was designed based on the specification given in Table 5. The experimental setup in the laboratory is presented in Figure 15(a) and the proposed TSBBM topology is presented in Figure 15(b). The same simulated PV module characteristic data were used for the experimental study using the chroma programmable DC power supply 62150H-600S solar array simulator. The programmable AC/DC electronic load 63802 was used for loading purposes. The grid was replicated using chroma 3-phase programmable AC source 61704. In the control section, the switching strategy has been developed in MATLAB and is interlinked with the dSPACE-1104 control desk. All the waveforms are obtained from DSOX3014 oscilloscope.

Figure 16 shows the switching pulses generated from the dSPACE-1104 through TLP350 gate driver. Here, SW_1 and SW_2 shows 50 kHz pluses, whereas SW_3 and SW_4 shows 50 Hz pulses as explained in the theory. Figure 17 shows currents through L_P and L_N during $1 \text{ kW}/\text{m}^2$ irradiation level. It clearly validates the DCM operation of the inverter and $I_{L,Peak} \approx 6A$ during maximum power as mentioned in theoretical study. The output voltage and current with input voltage and current during steady state are displayed in the Figure 18. The RMS value of the output voltage and current is equal to the value designed and simulated. From Figure 18, the efficiency obtained is 96.4% as given in (44).

$$Efficiency(\%) = \frac{(109.84 \times 0.593)}{73.5 \times 0.95} \times 100 = 93.3\%. \quad (44)$$



(a)



(b)

FIGURE 15 (a): Complete experimental setup, (b): power circuit of TSBBM

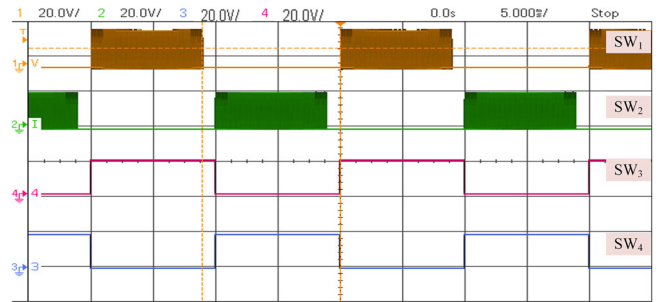


FIGURE 16 Switching pulses generated for TSBBM inverter

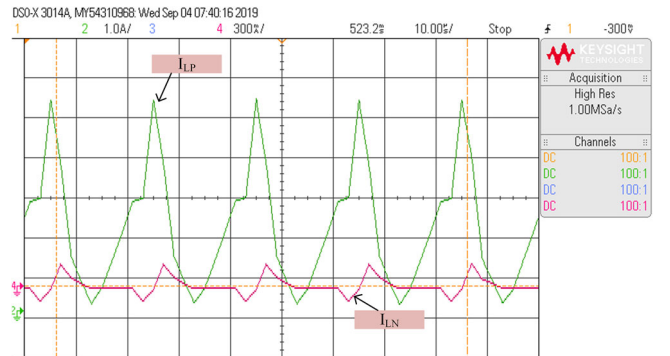


FIGURE 17 Inductor currents I_{Lp} and I_{Ln} at $1 \text{ kW}/\text{m}^2$ irradiation

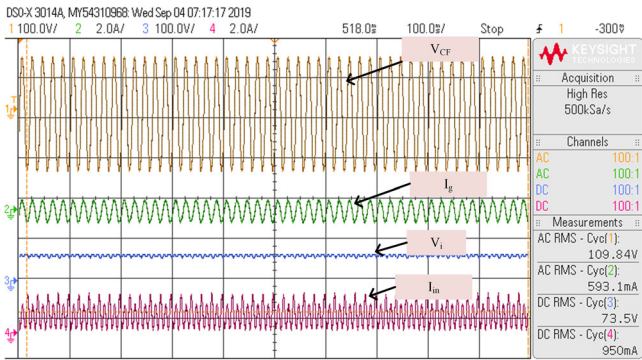


FIGURE 18 Steady state output and input voltage and current waveforms at $1 \text{ kW}/\text{m}^2$ irradiation

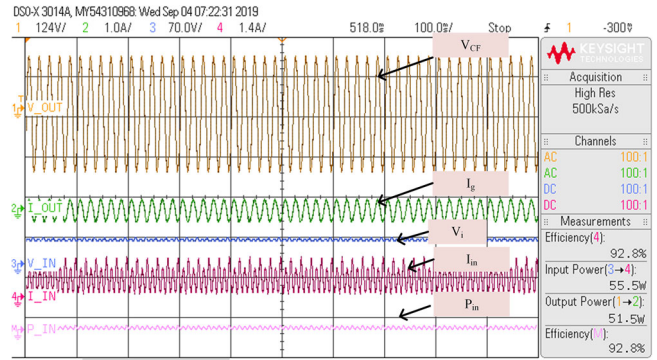


FIGURE 21 Output and input voltage and current with efficiency at $0.8 \text{ kW}/\text{m}^2$

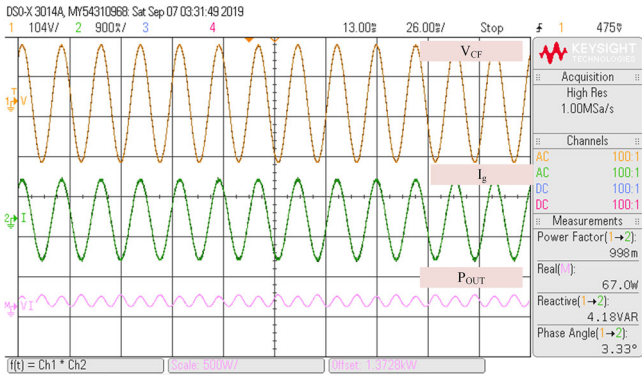


FIGURE 19 Power quality measurements at $1 \text{ kW}/\text{m}^2$ irradiation

Figure 19 gives the power factor, real power, reactive power and phase angle with generated voltage, current and apparent power waveforms at $1 \text{ kW}/\text{m}^2$ irradiation. It clearly shows that the power factor is ≈ 1 . The Fast Fourier Transform (FFT) and Total Harmonic Distortion (THD) value of the injected current from the inverter appear in Figure 20. The current fed to the grid has a THD value approximately equal to 4%. Figure 21 shows the steady state output and input voltage and current at $0.8 \text{ kW}/\text{m}^2$ irradiation with efficiency calculation. In Figure 22, the inverter efficiency curve for different input voltages is

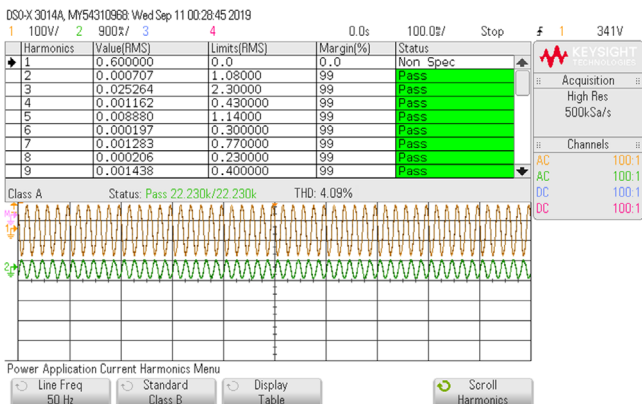


FIGURE 20 THD of injected current at $1 \text{ kW}/\text{m}^2$ irradiation

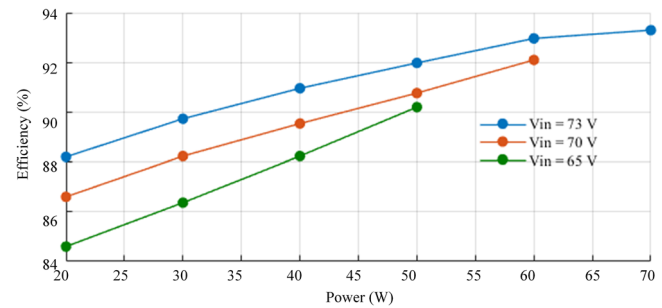


FIGURE 22 Efficiency curve of the proposed inverter

illustrated. In order to identify the variation in the efficiency of the proposed topology when working from low to rated power, it is conducted by means of a DC source and resistive load.

6.3 | Comparison of topologies

The review of the various micro-inverters is presented in the Table 6. All inverters are simulated for 70 W using PLECS software with the same benchmark as the proposed topology [23]. Efficiency, THD of injected current and leakage current of all topologies have been identified. The size of the inverters is determined using the Eagle software based on the circuit board required for the power circuit. Based on the number of components used, cost of the topologies are compared. The loss break down of each topology based on the same benchmark is shown in the Figure 6. The [18] and [29] is more efficient than the proposed topology while observing number of components in conduction path and size of the topology the proposed topology shows an optimized microinverter for BIPV application. In addition to this point, fewer sensors are used in the topology, which reduces the cost of the system further. As a whole, TSBBM topology is efficient and has minimal active, passive and sensor components, making the topology suitable for applications involving BIPV.

TABLE 6 Comparison of different topology

Topology	No. of components in conduction path				Efficiency	SS	THD	Leakage current (mA_{RMS})	Cost	Size (cm^2)
	SW	D	L	C						
[28]	2	2	1	1	Moderate	1944.3	$\leq 5\%$	≤ 30	Moderate	102.18
[14]	2	2	2	2	Moderate	2208.5	$\leq 5\%$	≥ 30	Moderate	160.00
[15]	3	1	1	1	Moderate	1253.7	$\leq 5\%$	≥ 30	High	80.36
[16]	2	0	2	1	High	979.1	$\leq 5\%$	≤ 30	High	203.17
[17]	3	0	2	1	low	1269	$\leq 5\%$	≥ 30	High	203.44
[18]	3	1	2	2	Very high	1154.7	$\leq 5\%$	≥ 30	High	203.18
[29]	2	2	2	2	Very high	876.36	$\leq 5\%$	≤ 30	High	200.61
[19]	3	0	2	2	low	2530.2	$\leq 5\%$	≤ 30	Moderate	116.82
[20]	2	0	1	1	High	1379.1	$\leq 5\%$	≤ 30	Moderate	105.39
[30]	2	0	2	2	High	1104.4	$\leq 5\%$	≤ 30	Moderate	128.25
TSBBM	1	1	1	1	Very high	972.3	$\leq 5\%$	≤ 30	Moderate	120.6

Very high – $\eta > 90\%$, High – $80\% < \eta \leq 90\%$, Moderate – $70\% < \eta \leq 80\%$, Low – $\eta \leq 70\%$

7 | CONCLUSION

TSBBM with a lower number of passive and active elements has been proposed in this paper. Without a specialized DC–DC converter or step-up transformer, the desired voltage gain was achieved. High performance and cost reductions are obtained due to the minimal number of components. Simulation and experimental performance verified the design methodology for all passive elements of the inverter and current sensorless control of the system. A comparative study of the proposed inverter, with identical topologies, shows that the TSBBM had negligently low leakage current, high operating efficiency, allowable THD levels for the current injected, prevented shoot-through problems and no current sensors. TSBBM can therefore be recommended as an efficient system to be used and marketed as an interface device for BIPV applications.

ORCID

Derick Mathew  <https://orcid.org/0000-0001-5930-5077>

REFERENCES

- Eder, G., et al.: Coloured bipv: Market, research and development. Report IEA-PVPS T15-07: 2019
- Ballif, C., et al.: Integrated thinking for photovoltaics in buildings. *Nature Energy* 3(6), 438 (2018)
- Kan, J., et al.: Hybrid control scheme for photovoltaic micro-inverter with adaptive inductor. *IEEE Trans. Power Electron.* (2018)
- Rajeev, M., Agarwal, V.: Single phase current source inverter with multi-loop control for transformerless grid–pv interface. *IEEE Trans. Ind. Appl.* 54(3), 2416–2424 (2018)
- Strache, S., et al.: A comprehensive, quantitative comparison of inverter architectures for various PV systems, PV cells, and irradiance profiles. *IEEE Trans. Sustain. Energy* 5(3), 813–822 (2014)
- Gagrica, O., et al.: Microinverter curtailment strategy for increasing photovoltaic penetration in low-voltage networks. *IEEE Trans. Sustain. Energy* 6(2), 369–379 (2015)
- Sher, H.A., et al.: An efficient and cost-effective hybrid MPPT method for a photovoltaic flyback microinverter. *IEEE Trans. Sustain. Energy* 9(3), 1137–1144 (2017)
- Jeong, Y.S., et al.: High-efficiency bidirectional grid-tied converter using single power conversion with high-quality grid current. *IEEE Trans. Ind. Electron.* 64(11), 8504–8513 (2017)
- Alluhaybi, K., et al.: Comprehensive review and comparison of single-phase grid-tied photovoltaic microinverters. *IEEE Journal of Emerging and Selected Topics in Power Electronics* (2019)
- Jha, K., et al.: High-quality sine wave generation using a differential boost inverter at higher operating frequency. *IEEE Trans. Ind. Appl.* 51(1), 373–384 (2014)
- Melo, F.C., et al.: Proposal of a photovoltaic ac-module with a single-stage transformerless grid-connected boost microinverter. *IEEE Trans. Ind. Electron.* 65(3), 2289–2301 (2017)
- Ardashir, J.F., et al.: A single-phase transformerless inverter with charge pump circuit concept for grid-tied PV applications. *IEEE Trans. Ind. Electron.* 64(7), 5403–5415 (2016)
- Kasa, N., Iida, T., Iwamoto, H.: Maximum power point tracking with capacitor identifier for photovoltaic power system (2000)
- Piazza, G.L., Barbi, I.: New step-up/step-down DC-AC- converter. *IEEE Trans. Power Electron.* 29(9), 4512–4520 (2013)
- Tang, Y., et al.: Active buck–boost inverter. *IEEE Trans. Ind. Electron.* 61(9), 4691–4697 (2013)
- Tamyurek, B., Kirimer, B.: An interleaved high-power flyback inverter for photovoltaic applications. *IEEE Trans. Power Electron.* 30(6), 3228–3241 (2014)
- Sreekanth, T., et al.: A single-stage grid-connected high gain buck–boost inverter with maximum power point tracking. *IEEE Trans. Energy Convers.* 32(1), 330–339 (2016)
- Khan, A.A., et al.: A highly reliable and high-efficiency quasi single-stage buck–boost inverter. *IEEE Trans. Power Electron.* 32(6), 4185–4198 (2016)
- Gautam, V., Sensarma, P.: Design of cuk-derived transformerless common-grounded PV microinverter in CCM. *IEEE Trans. Ind. Electron.* 64(8), 6245–6254 (2017)
- Azary, M.T., et al.: Modified single-phase single-stage grid-tied flying inductor inverter with MPPT and suppressed leakage current. *IEEE Trans. Ind. Electron.* 65(1), 221–231 (2017)

21. Kumar, A., Sensarma, P.: New switching strategy for single-mode operation of a single-stage buck–boost inverter. *IEEE Trans. Power Electron.* 33(7), 5927–5936 (2017)
22. Ahmed, J., Salam, Z.: An enhanced adaptive P&O MPPT for fast and efficient tracking under varying environmental conditions. *IEEE Trans. Sustain. Energy* 9(3), 1487–1496 (2018)
23. Mathew, D., Naidu, R.C.: Investigation of single-stage transformerless buck–boost microinverters. *IET Power Electron.* 13(8), 1487–1499 (2020)
24. Derick, M., et al.: An improved optimization technique for estimation of solar photovoltaic parameters. *Solar Energy* 157, 116–124 (2017)
25. Mathew, D., et al.: Wind-driven optimization technique for estimation of solar photovoltaic parameters. *IEEE J. Photovolt.* 8(1), 248–256 (2017)
26. Freddy, T.K.S., et al.: Comparison and analysis of single-phase transformerless grid-connected PV inverters. *IEEE Trans. Power Electron.* 29(10), 5358–5369 (2013)
27. Melo, F.C., et al.: Proposal of a photovoltaic AC-module with a single-stage transformerless grid-connected boost microinverter. *IEEE Trans. Ind. Electron.* 65(3), 2289–2301 (2017)
28. Patel, H., Agarwal, V.: A single-stage single-phase transformer-less doubly grounded grid-connected PV interface. *IEEE Trans. Energy Convers.* 24(1), 93–101 (2009)
29. Khan, A.A., Cha, H.: Dual-buck-structured high-reliability and high-efficiency single-stage buck–boost inverters. *IEEE Trans. Ind. Electron.* 65(4), 3176–3187 (2017)
30. Kumar, A., Sensarma, P.: A four-switch single-stage single-phase buck–boost inverter. *IEEE Trans. Power Electron.* 32(7), 5282–5292 (2016)

How to cite this article: Mathew D, et al.: Single-stage microinverter with current sensorless control for BIPV system. *IET Renew Power Gener.* 2021;1–12.
<https://doi.org/10.1049/rpg2.12177>